1   **Intrinsic fluorescence in non-aromatic peptide structures is induced by collective**

2   **vibrations, charge reorganisation and short hydrogen bonds, as shown in a new**

3   **glutamine-related structure**

4

5   Amberley D. Stephens,*[1] Muhammad Nawaz Qaisrani,*[2,3] Michael T. Ruggiero,[4,1] Saul T.E.

6   Jones,[5] Emiliano Poli,[2] Andrew D. Bond,[6] Philippa J. Woodhams,[1] Elyse M. Kleist,[7] Luca

7   Grisanti,[8] Ralph Gebauer,[2] J. Axel Zeitler,[1] Dan Credgington,[5] Ali Hassanali,[2#] Gabriele S.

8   Kaminski Schierle[1#]

9

10

11   [1] Chemical Engineering and Biotechnology, University of Cambridge, Cambridge CB3 0AS, UK
12   [2] The Abdus Salam International Centre for Theoretical Physics, Strada Costiera 11, 34151 Trieste,
13   Italy
14   [3] International School for Advanced Studies, Via Bonomea 265, 34136 Trieste, Italy
15   [4] Department of Chemistry, University of Vermont, 82 University Place, Burlington, VT, 05405 USA
16   [5] Cavendish Laboratory, University of Cambridge, JJ Thomson Avenue, Cambridge, CB3 0HE, U.K
17   [6] Department of Chemistry, University of Cambridge, Lensfield Road, Cambridge CB2 1EW, United
18   Kingdom
19   [7] Department of Chemistry, Syracuse University, Syracuse, New York 13244, United States
20   [8] Division of Theoretical Physics, Ru¯der Boškovi´c Institute, Bijeni˘cka cesta 54, 10000 Zagreb,
21   Croatia
22   * Contributed equally
23   # Corresponding authors: ahassana@ictp.it, gsk20@cam.ac.uk
24

25

26   **Abstract**

27   Disentangling the origin of the optical activity of non-aromatic proteins is challenging due to

28   their size and thus their high computational requisites. Here we show, in a much smaller

29   model system, that the single amino acid glutamine undergoes a chemical transformation

30   leading to an unreported glutamine-like structure which has a similar broad absorption

31   spectrum reported previously for non-aromatic proteins. We further show computationally

32   that the optical activity of the glutamine-like structure is directly coupled to short-hydrogen

33   bonds, but also displays charge and vibrational fluctuations, the latter of which are also

34   present in less optically active structures such as in L-glutamine. Since experimentally the

35   glutamine-like structure is the brightest structure, we conclude that short-hydrogen bonds

36   are the ones responsible for the large Stokes shift observed in optically active non-aromatic

37   proteins.

38   **Introduction**

39

40   Short peptides void of any aromatic residues have been shown to display an intrinsic

41   fluorescence in the visible range (*1, 2*). This has primarily been observed in fibrillar protein

42   structures linked to neurodegenerative diseases, such as Alzheimer's, Parkinson's and

43   Huntington's diseases (*3–6*). Furthermore, optical properties of double amino acid based

44   nanowires have also been reported, existing either of two non-aromatic or two aromatic

45   amino acids (*2, 7, 8*). We have shown that the fluorescence of non-aromatic short crystal

46   structures forming part of the amyloid-beta protein is enhanced by the presence of short

47   hydrogen bonds (SHB) between the termini of prefibrillar structures (*5*). The SHB permits

48   proton transfer leading to a double-well ground state potential which we have proposed

49   prevents a conical intersection in the excited state (*5*). It has been suggested that one of the

50   prerequisites for this fluorescence observed in either amyloid structures or short peptide

51   nanowires is related to hydrogen bonding or aromatic interlocks which, for the latter,

52   decreases the bandgaps down to the semiconductive regions (*9*).

53

54   Despite our previous suggestion that proton delocalisation is strongly coupled to this

55   intrinsic fluorescence, its direct role and more importantly, the role of other vibrational

56   modes on putative fluorescing states, has not been elucidated. We have thus searched for a

57   model system, such as a single amino acid-based structure, that displays similar optical

58   properties to amyloid fibrils and is permissive to more sophisticated computational

59   approaches. We have been inspired by the small peptide nanostructures that have been

60   pioneered by the Gazit laboratory (*9*) and by the fact that there are several

61   neurodegenerative diseases that have been connected with an increased level of glutamines

62   produced as part of a protein, as for example Huntingtin in Huntington's disease which

63   renders the protein more aggregation prone (*10*). It has been known that the amide group

64   in L-glutamine (L-glu) is highly labile and thus can rapidly hydrolyse. We show here that the

65   single amino acid L-glu upon heating in water can form a nanostructural material with

66   optical properties similar to the ones observed in other amyloid fibrils such as in fibrils of

67   amyloid-beta, alpha-synuclein or tau (*4, 11, 12*).

68

69   Using X-ray diffraction (XRD), we show that L-glu dissolved in water and upon heating

70   becomes cyclysed forming a previously unreported structure which resembles L-

71   pyroglutamine (which has been reported to be a component of amyloid-beta in the brain

72   (*13*)), but involves a low-barrier hydrogen bonded anionic dimer with an ammonium

73   counterion. We have termed the new structure, i.e. L-pyroglutamine complexed with an

74   ammonium ion, L-pyro-amm. L-pyro-amm has a microcrystalline plate morphology as shown

75   by scanning electron microscopy (SEM). The newly formed solid was further characterised

76   using terahertz time-domain spectroscopy (THz-TDS), which provides information on the

77   low-frequency modes in the crystal that control the proton transfer. Additionally, the

78   experiments were interpreted using ground and excited state electronic structure

79   calculations and molecular dynamics simulations. Ultimately, the combination of static

80   structural information, atomic vibrational dynamics, and optical properties enable the

81   origins of fluorescence in this particular structure to be elucidated, shedding light on the

82   complementary processes in more complex systems.

83

84   **Methods**

85

86   *Experimental*

87   *Sample preparation of L-glutamine*

88   L-glutamine (L-glu) (#G3126, #G8540, Sigma-Aldrich, Gillingham, UK) and L-pyroglutamine

89   (L-pyro) (#83160, Sigma-Aldrich) were dissolved in 18.2Ω MilliQ H_2O at a concentration of

90   0.3 M or 1 M. Aliquots were placed in a 65°C oven, since heating up proteins to 65°C

91   increases the formation of amyloid structures as reported previously (*14*). Each aliquot was

92   rotated to dissolve the powder once a day. Samples were either analysed in liquid form or

93   dried on a glass or quartz cover slip (#043210.KG, Alfa Aesar, Lancashire, UK) either at room

94   temperature (RT) or on a heat block set to 50°C.

95

96   *Emission and excitation wavelength scans*

97   Emission and excitation spectra were taken on a Hitachi F-4500 FL spectrophotometer

98   (Hitachi High-Technologies Corporation, Tokyo, Japan) at RT in a quartz cuvette. For

99   measurements, the excitation slit resolution was 5 nm or 10 nm and the emission slit

100   resolution was 20 nm. The PMT voltage was set at 950 V and the scan speed set at 240

101   nm/min. The excitation scan was measured between 250 – 400 nm and the emission filter

102   set to the emission maxima of the sample stated in the figure legend, with a slit resolution

103   of 20 nm. The emission scan was measured between 380 - 560 nm and the excitation filter

104   set to the excitation maxima of the sample stated in the figure legend, using a slit resolution

105   of 5 nm. Four measurements were taken for each sample which was repeated at least three

106   times and the background (air or H_2O) was subtracted from the average.

107

108   *Absorption measurements*

109   Absorption measurements were taken on a UV-Vis-NIR Spectrophotometer, UV-3600 Plus

110   (Shimadzu, Kyoto, Japan) and Cary 6000i (Agilent, Santa Clara, USA). 1 M or 0.3 M L-glu, L-

111   pyro or L-pyro-amm solutions were measured in 10 mm QX cuvettes (Hellma Analytics,

112   Müllheim, Germany) or dried on quartz coverslips. Measurements were taken between

113   wavelengths 200 – 800 nm using 1 nm steps at a slow scan speed and a 1 nm resolution. The

114   light source change wavelength was set at 393 nm and the grating change wavelength set at

115   750 nm. Samples were measured at least three times and the experiments repeated at least

116   three times, measurements were then averaged and H_2O or coverslip only control was

117   subtracted.

118

119   *SEM (scanning electron microscopy)*

120   SEM was performed using a FEI Magellan 400 HR-SEM at an acceleration voltage of 2 kV. L-

121   pyro-amm samples were lyophilised by freezing in liquid nitrogen and freeze drying in a

122   LyoQuest 85 (Telstar, Terrassa, Spain) and imaged on a glass coverslip.

123

124   *X-ray diffraction*

125   L-pyro-amm was dried on a glass coverslip in a 50°C oven and then at RT until crystals

126   formed. Single crystal X-ray diffraction (SCXRD) measurements were performed at 180 K

127   with a Bruker D8-QUEST PHOTON-100 diffractometer, which utilised a Cu Kα radiation (λ =

128   1.54 Å), and an APEX-II CCD. Absorption corrections were made using SDABS, and data

129   integration and reduction were performed with SAINT+. All non-hydrogen atoms were

130   refined isotropically and anisotropically, followed by inclusion of the hydrogen atoms

131   (determined using the excess electron density) and refinement isotropically.

132

4

133   *Terahertz Time-Domain Spectroscopy*

134   All THz-TDS spectra were acquired using a commercial Terapulse 4000 spectrometer

135   (TeraView Ltd, Cambridge, UK). Samples were prepared for THz-TDS measurements by

136   diluting the solid air dried L-pyro-amm with polyethylene (~ 10% w/w concentration) by

137   gentle mixing using an agate mortar, followed by pressing into 2 mm thick, 13 mm diameter

138   pellets using a hydraulic press. All THz-TDS spectra shown are a result of division of sample

139   and blank datasets, with the blank dataset represented the THz-TDS response of a pellet of

140   pure polyethylene.

141

142   *Theoretical*

143   *DFT-THz Calculations*

144   Calculations were performed using both the CRYSTAL17 (*15*) and Quantum Espresso (*16*)

145   software packages. Geometry optimisations and vibrational analyses performed with the

146   CRYSTAL17 code utilised the atom-centred split-valence triple-zeta 6-311g(2d,2p) basis set

147   for all atom types. Based on a previous study related to ionic molecular crystals (*17*), the

148   range-corrected WB97-X (*18*) functional was used. The vibrational analysis was performed

149   within harmonic approximation, and infrared intensities were determined using the Berry

150   Phase method. Energy convergence criteria were set to $\Delta E < 10^{-8}$ and 10^{-11} hartree for the

151   geometry and frequency calculations, respectively.

152

153   *Periodic TD-DFT Excited State Calculations*

154   Simulations were performed using the fully periodic Quantum Espresso software package.

155   The Becke-Lee-Yang-Parr (B3LYP) hybrid density functional was used with an energy cutoff

156   of 40 Ry. The calculations of the excited state were performed within the framework of

157   TDDFT using the Liouville-Lanczos formalism implemented in the freely available Quantum-

158   Espresso package (*19*). In this approach, the optical spectra are obtained directly over the

159   wide spectral range without taking into account the numerically complex calculations of the

160   single exited states. We used plane wave basis set and the electron-ion interactions were

161   taken into account via norm conserving Martins-Troullier pseudopotentials (*20*). To

162   determine the ground state wave function, we used the gamma point of the Brillouin zone.

163   All the periodic calculations employed the computationally demanding B3LYP (*21*) hybrid

164   functional, the kinetic energy cutoff of 40 Ry was used for the wave functions. The intrinsic

165   band width for the spectra was set to 0.003 Ry (~0.0408 eV).

166

167   *Periodic Structure Geometry Optimisation*

168   The structures obtained from the experiments were first geometrically optimized at $0°K$

169   using the Broyden-Fletcher-Goldfarb-Shanno (BFGS) minimisation algorithm implemented in

170   CP2K (*22, 23*) package. A convergence criterion for the wave function optimisation was used

171   as $5x10^{-7}$ a.u. Applying the method of the Gaussian and plane wave, the wave function was

172   expended in the Gaussian double-zeta valence polarised (DZVP) basis set. The cutoff for the

173   electronic density was set to 300 Ry. We used the gradient correction to the local density

174   approximation and the core electrons were treated via Goedecker-Teter-Hutter

175   pseudopotentials (*24*). In all the calculations, we used the Becke-Lee-Yang-Parr (BLYP) (*25*)

176   functional with the D3(0) Grimme (*26*) dispersion corrections for the van der Waals

177   interactions.

178

179   *Ab Initio Molecular Dynamics Simulations*

180   Ab initio Molecular Dynamics simulations (AIMD) were performed using Quickstep

181   algorithm implemented in CP2K. In these calculations, the propagation of the nuclei was

182   taken into account within the framework of the Born-Oppenheimer approximation. The

183   simulations were performed in the NVT ensemble and the temperature was controlled

184   during the simulations by using the velocity-rescaling thermostat (*27*). We used the time

185   step of 0.5 femtosecond to update the nuclear coordinates and velocities while the total

186   length of the simulations for each system is 50 picoseconds.

187

188   *Excited State Cluster Calculations*

189   A set of excited state calculations were performed on glutamine clusters in order to

190   understand the role of the environment on the optical properties. Specifically, the optical

191   properties of L-pyro-amm were investigated using various isolated cluster models with the

192   Gaussian09 software package. The clusters were extracted directly from the crystal

193   structure and used in various combinations (dimers, trimers, tetramers) to perform time-

194   dependent DFT (TD-DFT) calculations. A split-valence triple-zeta 6-311g(2d,2p) basis set was

195   used for all atom types together with the hybrid B3LYP functional. Some benchmark

6

196   simulations, comparing the optical properties obtained from the periodic calculations using

197   B3LYP to range corrected hybrid functionals like CAM-B3LYP, were also performed with

198   these clusters.

199

200   We also performed a series of excited state optimisations on various model systems built

201   from L-pyro-amm in order to examine the nature of the geometrical distortions that occur

202   on the lowest electronic excited state. These calculations were also performed with the

203   Gaussian09 software package. All clusters were surrounded with a continuum dielectric

204   constant of 80, representing pure H_2O. The 6-311G(2d,2p) basis set was used for all atoms

205   together with the range corrected hybrid functional CAM-B3LYP (28). The clusters were first

206   optimised in the ground state after which they were optimised on the first electronic

207   excited state.

208

209   **Results and Discussion**

210

211   It has long been known that poly-glutamine can form amyloid-like fibrillar structures *in vitro*.

212   The more glutamine residues in the poly-glutamine polymer, the faster the aggregation

213   propensity of the polypeptide chain. This led us to investigate whether L-glu on its own

214   under conditions which normally promote fibril formation, such as an increase in

215   temperature (14), was able to form structures with similar optical properties, as recently

216   observed for amyloid fibrils (5, 29, 30).

217

218   We first investigated the structure of L-pyro-amm, which formed after incubation of L-glu

219   for 8 days at 65°C, using SEM and observed crystal structures shown in Fig.1a. However, in

220   order to investigate whether L-glu had indeed changed its crystal structure arrangement we

221   performed XRD analysis of the resulting material. In Fig.1b we show the crystal structure of

222   the heated L-glu structure, which we termed L-pyro-amm, and the published crystal

223   structures of L-glu and L-pyroglutamine (L-pyro) in Fig. 1c and d. Note, the L-pyro structure

224   was analysed as it displayed structural similarities to the newly formed L-pyro-amm. Figures

225   were obtained from geometry optimisations of the nuclear positions of the atoms using

226   experimental densities. L-pyro-amm consists of 8 pyroglutamine groups and 4 ammonium

227   ions (144 atoms) complexed within the crystal (see Fig. 1b). In contrast, as shown in Fig. 1c,

228   L-glu consists of 4 glutamine molecules (80 atoms) in the unit cell which form hydrogen
229   bonds involving the termini and side chain. Furthermore, as shown in Fig. 1d, L-pyro consists
230   of 12 pyroglutamine molecules (192 atoms) in the unit cell forming hydrogen bonds
231   involving the NH and COOH groups.

232

233   L-pyro-amm has a rather unique hydrogen bond network structure since four of the
234   pyroglutamine molecules are deprotonated and hence have a nominal negative charge,
235   while the other four molecules are neutral. One of the important implications of this
236   difference is that L-pyro-amm contains a very strong hydrogen bond. The red circled region
237   in Fig. 1a corresponds to a short hydrogen bond (SHB) with a length of 2.45 Å, while those in
238   L-glu and L-pyro range between ~2.55-2.85 Å.

239

240   The structural change was further confirmed using THz-TDS measurements, as this
241   technique is strongly dependent on the bulk packing arrangement (as well as on the internal
242   covalent structure) of the molecules (*31*). The THz-TDS spectrum of the resulting solid, as
243   well as the solid-state DFT predicted spectrum based on the single crystal XRD (SCXRD)-
244   determined structure, is shown in Fig. 1e (full spectral assignment available in Suppl. Fig. 1).
245   The agreement between the experimental and theoretical spectra further supports that full
246   conversion of the sample occurs and thus enables additional investigations into the
247   structural and electronic properties of the material.

248
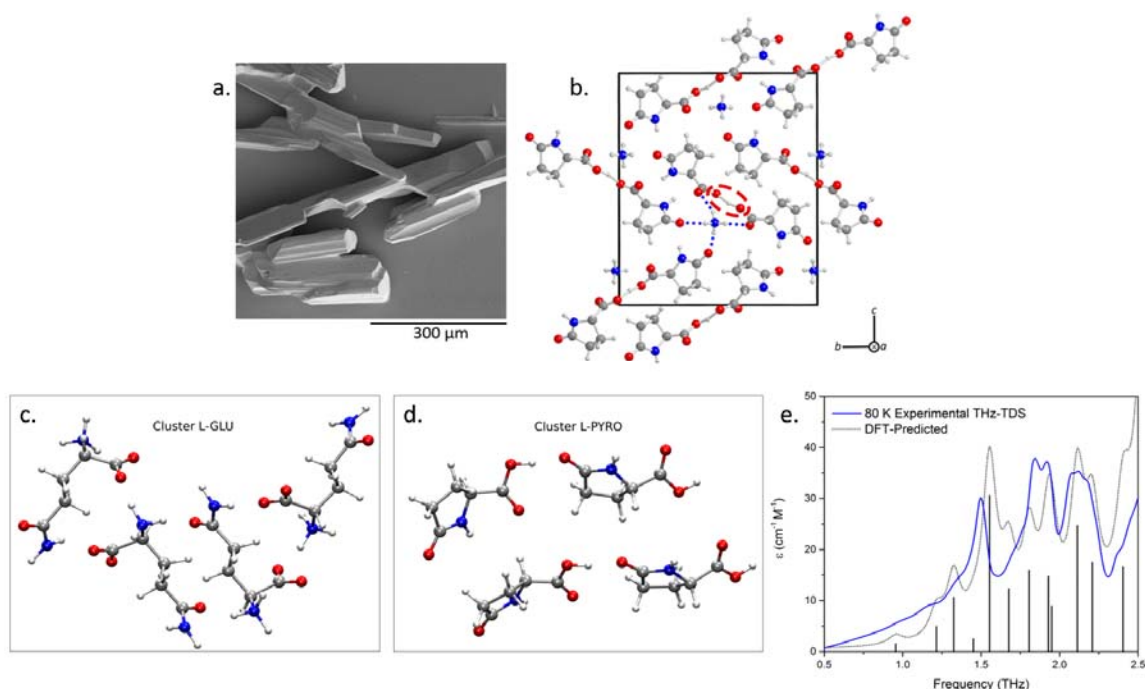
Figure 1. L-glu forms L-pyro-amm upon heating.

(a) SEM image of crystals of L-pyro-amm dried. (b) XRD analysis of heated L-glu sample show the newly formed structure, L-pyro-amm. Geometry optimisations show that 8 pyroglutamine groups and four ammonium ions (144 atoms) are complexed in the crystal and a SHB of 2.45 Å (within red dashed lines) is present near the ammonium ion (linked by bonds highlighted by blue dotted lines) (white-hydrogen, red-oxygen, blue-nitrogen, grey-carbon). (c) Clusters of L-glutamine and (d) L-pyroglutamine. (e) Experimental (blue line) and theoretical (grey line) THz-TDS of the L-pyro-amm sample are in agreement and confirm the presence of the new L-pyro-amm structure.

We first investigated whether there were any differences in the optical properties associated with the three crystal structures. Comparing the absorption of L-glu, L-pyro and L-pyro-amm in water, we show that only L-pyro-amm has a significantly red-shifted absorption which lies in the 275-320 nm range, whereas both L-glu and L-pyro primarily absorb in the deep UV (<250 nm) (see Fig. 2a).

We next compared the experimental absorption spectra of L-glu, L-pyro and L-pyro-amm with the ones obtained from time dependent density functional theory (TDDFT). We highlight here, that the small size of the systems permitted us to determine the spectra

268   using a hybrid functional, thereby not only advancing the quality of our theoretical

269   predictions from previous studies (*5*, *29*, *30*) but also coupling the optical properties directly

270   to different vibrational modes.

271

272   Fig. 2b illustrates the absorption spectra obtained for the TDDFT calculations on the 3

273   periodic systems in the ground state (i.e. at 0 K). Panel b.i) shows the relative oscillator

274   strength as a function of the frequency while panel b.ii) illustrates the second derivative of

275   the oscillator strength permitting the positions of the maxima in the spectra to be more

276   easily identified. The spectra reveal some striking differences between the different

277   systems. Interestingly, we observe that L-pyro is essentially dark throughout the frequency

278   range up to ~6eV. On the other hand, L-pyro-amm shows the presence of more structure in

279   the spectrum. Specifically, it is the only system for which the spectrum features a low

280   energy excitation at 226 nm (5.5 eV) and subsequently other peaks slightly above 220 nm

281   (5.625eV) and 216 nm (5.75eV). While L-glu exhibits a peak at 222 nm (5.58eV), it is dark up

282   to 206 nm (~6eV). These calculations were performed with the B3LYP functional.

283   Importantly, we have found that upon using more accurate functionals such as CAM-B3LYP

284   (*28*) and WB97-X (*18*) L-pyro-amm remains the most optically active.

285

286   We have previously shown that thermal fluctuations and in particular nuclear vibrations,

287   such as proton transfer, have a large impact on the absorption spectra of peptide structures

288   compared to absorption spectra at 0 K (*5*, *32–34*). In Fig. 2c we show that, compared to the

289   0 K spectra in Fig. 2b, thermal fluctuations cause a large red shift to around 3.4 eV (365 nm)

290   for L-pyro-amm, close to what is observed experimentally. These spectra were computed

291   averaging over 25 frames sampled from the molecular dynamics simulations. Interestingly,

292   no such effect is observed for L-glu which remains weakly absorbing up to more than 5 eV

293   (247 nm) as seen at 0 K.

294

295   Similar to our previous studies on the intrinsic fluorescence of amyloid-beta fibrils,

296   absorption is significantly increased in structures containing SHB, as neither L-glu, nor L-pyro

297   display a significantly red shifted absorption. In order to understand better the physical

298   origin of the low energy excitation at 226 nm (~5.5 eV) in L-pyro-amm, we computed the

299   electron response density at this frequency. This is illustrated in Fig. 2d, where we observe

300   that most of the electron response involves regions around the pyroglutamine rings as well

301   as regions near the SHB (see dashed circle in Fig. 2d). The optical response thus involves a

302   collective charge reorganisation involving several parts of the molecular crystal.

303

304   We next investigated whether the above structures also display fluorescence excitation and

305   emission properties as has been observed for amyloid-like structures reported previously (5,

306   29, 30). Fig. 2e shows the excitation scan from 250-400 nm (solid lines) with the emission

307   set at 430 nm of L-glu in water at day 0 to 8 after incubation at 65°C. Interestingly, we

308   observe an excitation peak at around 360 nm which is similar to what we have measured

309   previously for amyloid proteins (5). The corresponding emission scan (dashed lines) with the

310   excitation set at 360 nm and emission from 380-560 nm showed an emission peak around

311   430 nm, again lying in the same visible range as for amyloid fibrils. When the L-pyro-amm

312   solution was dried the excitation and emission peaks were slightly blue shifted (Suppl. Fig.

313   2a) which may be due to a change in the molecular environment in the dried state.

314   Importantly, we do not see any fluorescence in L-glu (without heating, i.e. at day 0 Fig. 2e.).

315   To determine the importance of the ammonium ion experimentally, L-pyro has been

316   incubated in water and heated at 65°C for 8 days, and only a very weak fluorescence has

317   been detected (Suppl. Fig. 2b).
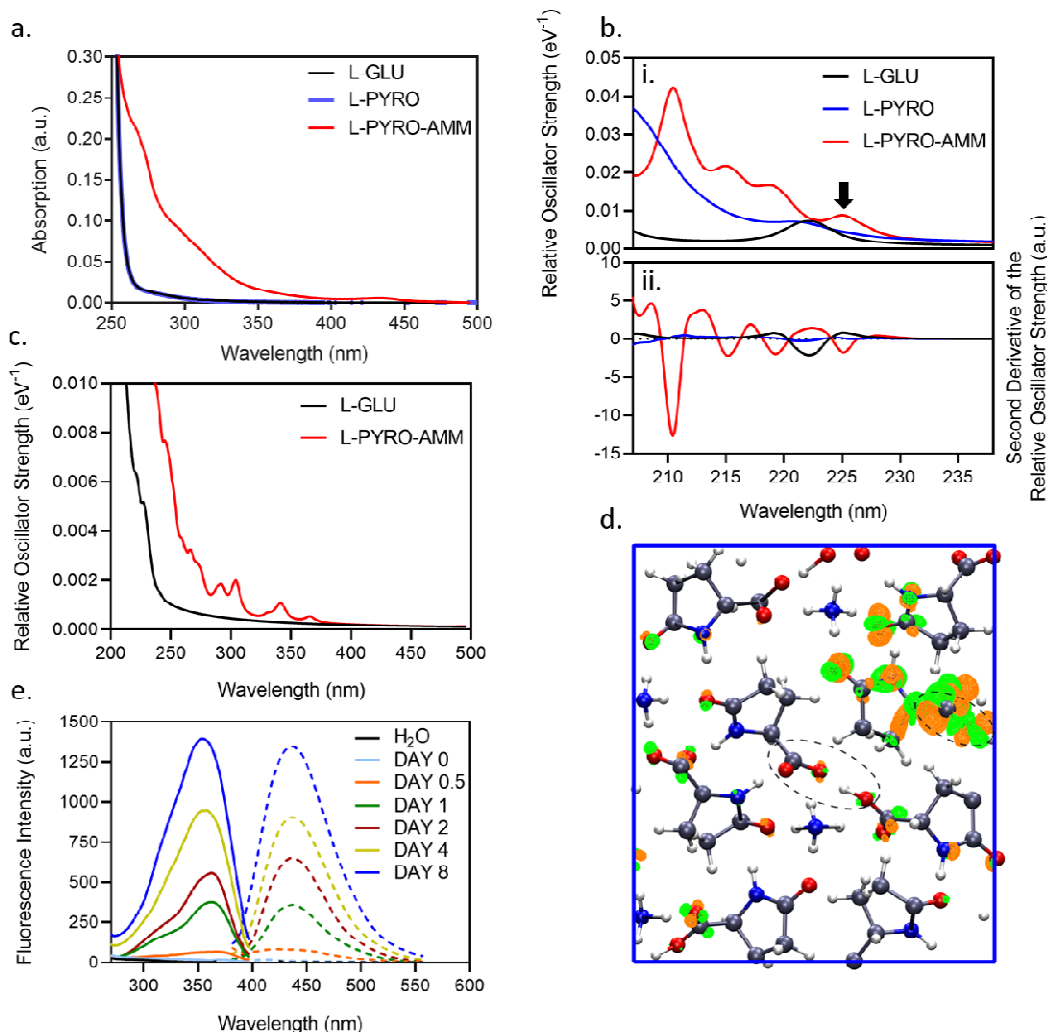
318
319 **Figure 2. Optical properties of L-pyro-amm are distinct from L-glu and L-pyro**

320 (a) Absorption spectra of 0.3 M L-glu (black), L-pyro (blue) and L-pyro-amm (red) (L-glu

321 incubated for 8 days at 65°C) in water taken between 200 – 500 nm shows primarily

322 features of L-pyro-amm. (b) Absorption spectra of L-glu, L-pyro and L-pyro-amm obtained

323 from periodic density functional theory calculations with the B3LYP functional. L-pyro-amm

324 features the lowest lying excited states which are characterised by the largest oscillator

325 strengths. (c) Absorption spectra for L-glu and L-pyro-amm obtained from periodic

326 simulations at room temperature. The spectra were computed by averaging over 25 frames

327 randomly sampled from the *ab initio* molecular dynamics simulations. (d) The excited state

328 electron density computed for L-pyro-amm from the optimised structure computed at the

329 first peak (arrow in panel b). The lowest excited state density shows a response from various

330 parts of the crystal structure including the pyroglutamic acid ring and the SHB region (see

331   dashed circle). The orange and green surfaces correspond to regions involving a decrease

332   and increase in electron density respectively, shown at an iso-value of 1×10^{-5}. (e) 1 M L-glu

333   was incubated at 65°C and the excitation and emission spectra were measured over time.

334   Excitation spectra were measured between 250-400 nm with emission set at 420 nm and

335   emission spectra were measured between 380-560 nm with the excitation set at 360 nm.

336

337   It is not possible to directly pinpoint the exact mechanisms and origins of the difference in

338   the optical properties between the three systems from the ground state calculations at 0 K.

339   As alluded to earlier, one of the factors that distinguishes L-pyro-amm from the other

340   systems is the presence of the SHB (highlighted by red circles in Fig. 1a) and the presence of

341   the ammonium ion. In order to characterise the behaviour of the SHB, we conducted *ab*

342   *initio* molecular dynamics simulations of the three systems at 300 K and examined the

343   proton transfer coordinates defined as the difference in distance between the proton (H)

344   and the two oxygen atoms (O1 and O2) that sandwich it and is commonly referred to as the

345   proton transfer coordinate ($d_{O1-H}-d_{O2-H}$) as shown in Fig. 4a for different types of hydrogen

346   bonds in the crystals. It is clear that the SHB in L-pyro-amm is characterised by a double-well

347   potential. The barrier associated with this proton transfer is on the order of thermal energy,

348   indicating that zero-point energy (ZPE) would make the proton transfer barrierless (*35*). An

349   examination of similar proton transfer coordinates for hydrogen bonds in L-glu and L-pyro

350   show that they are characterised by only single-well potentials.

351

352   The nature of the optical properties is sensitive to the environment in which the glutamine

353   molecules reside. It has previously been reported that charged amino acids already display

354   an absorption in the range of 250-350 nm that is significantly red shifted (*36, 37*). The

355   origins of the low energy absorption were attributed to charge transfer excitations. The

356   simulations of these systems were performed in the gas phase, rather than considering the

357   protein environment such as shown for L-pyro-amm in Fig 2d. In comparison to the results

358   presented in Fig. 2d, data presented in Fig. 3, show that the origins of the electronic

359   transitions equally arise from a charge transfer (CT) between the highest occupied

360   molecular orbital (HOMO) on the anionic dimer, and the lowest unoccupied molecular

361   orbital (LUMO) centred on the ammonium cation when performed in the gas phase.

362   Interestingly, the correct transition energy is only predicted when the ammonium cation is

363 spatially near the centre of the dimer, which corresponds to the delocalisation of the

364 negative charge and the SHB. Two generalised geometries, with the ammonium cation near

365 the SHB (as seen in Fig. 3a) and away from the SHB (Fig. 3b), with the corresponding HOMO

366 and LUMO orbitals are shown. The results predict a transition of 303.50 nm for dimer a. and

367 668.66 nm for dimer b., with dimer a. most closely resembling the chemical environment

368 present within the crystalline material.

369

370 The results show that charge transfer is capable to lead to absorption in the far UV when

371 investigated in the gas phase, i.e. neglecting the direct protein environment. However,

372 including the protein environment in the molecular crystal (Fig. 2d) results instead in the

373 excitation being a charge reorganisation involving several different molecular groups of the

374 crystal. Indeed, by shuffling the protons along the SHBs in the ground-state, we observe an

375 electronic response involving the entire structural units of L-pyro-amm including both the

376 hydrogen bonded regions and the pyroglutamic acid rings when the protein environment is

377 accounted for (Suppl. Fig.3b i-iv).
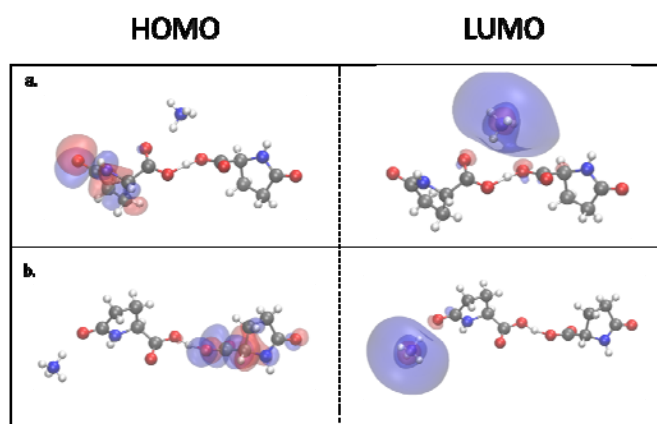
378

379 **Figure 3. Comparison of the HOMO and LUMO orbitals on two L-Pyro-Amm models.**

380 L-pyro-Amm structures are presented where the ammonium cation is located directly near

381 the hydrogen bond (a), and where the ammonium cation is located away from the hydrogen

382 bond (b). While both models predicted charge-transfer HOMO-LUMO states, only in the

383 case of (a) is the transition predicted to be in the vicinity of the experimentally observed

384 peak, 303.50 nm compared to 668.66 nm for (b).

385

386   Up to this point, we have shown that the vibrations of protons along SHBs are an important

387   part of the structural fluctuations in the ground state structure of L-pyro-amm. These

388   calculations however, do not say anything about the nuclear relaxation upon photo-

389   excitation which is most relevant for fluorescence. In a final set of theoretical studies, to

390   ascertain the role of the proton transfer in the ground state, as well as to elucidate the

391   presence of other types of vibrational modes, we performed a series of geometry

392   optimisations on the first excited state of a cluster carved out from L-glu, L-pyro and L-pyro-

393   amm crystals and surrounded by a continuum dielectric constant of 80.

394

395

396

15
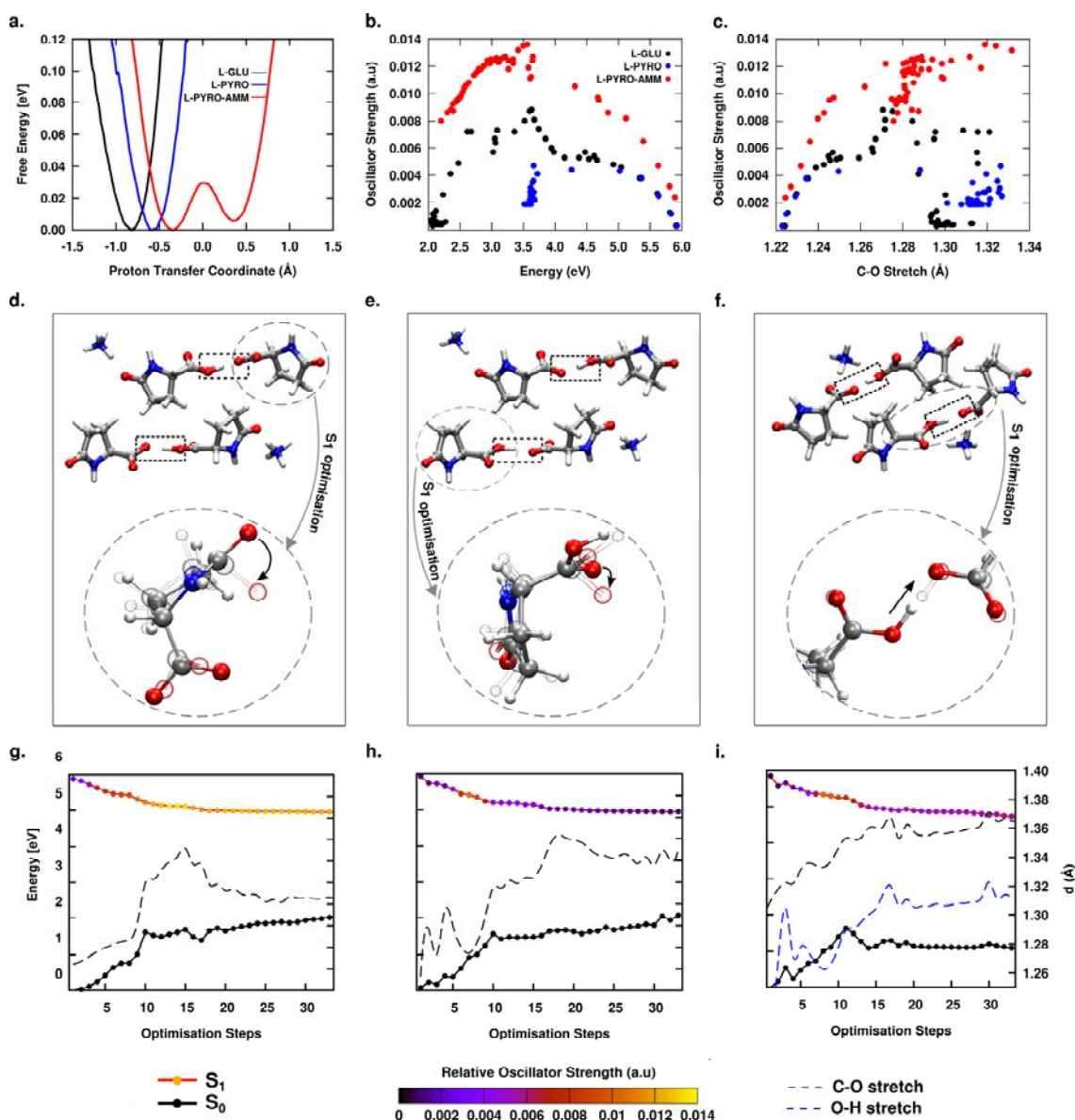
397 **Figure 4. Collective vibrations affect the emission in L-pyro-amm**

398 a) Shows the proton transfer free energy profiles along several hydrogen bonds in L-glu, L-

399 pyro and L-pyro-amm obtained from ground-state ab initio molecular dynamics simulations.

400 Note, the SHB in L-pyro-amm is characterised by a double-well potential. b) Scatter plot of

401 the oscillator strengths versus the emission energy (defined as the difference between the

402 first excited state and the ground-state) during the excited optimisations for L-glu, L-pyro

403 and L-pyro-amm. c) Scatter plot of the oscillator strengths versus the distance of the

404 carbonyl bond (C=O) that extends during the excited state optimisation in L-glu, L-pyro and

405 L-pyro-amm. d)-f) Snapshots of three different systems of L-pyro-amm that were optimised

406 on the excited state. In clusters shown in d) and e) the initial position of the proton along

407 the SHB has been changed, and in f) the ammonium ion has been placed closer to the SHB

408 region. The bottom panel of d), e) and f) show zoomed in plots of the main regions of the

409 cluster (circled in the top panels) that undergo significant changes. g)-i) Ground and excited

410 state energies are plotted as a function of the excited state optimisation for the three

411 systems shown in panels d-f). The curves on the excited state are colour-coded with the

412 oscillator strengths. S_0 and S_1 refer to the ground and excited state energies, respectively.

413 The right-side of the y-axis corresponds to C=O bond lengths (dashed black lines) for g) and

414 h). In panel i), where there is a proton transfer on the excited state, the dashed blue lines

415 correspond to the O-H distance along the SHB on the same distance scale.

416

417 Fig. 4b shows a scatter plot of the difference between the first excited state and ground-

418 state energies and the corresponding oscillator strengths. The scatter plots were obtained

419 over the course of the excited state optimisation. We observe that the L-pyro-amm system

420 is characterised by the largest oscillator strengths compared to L-glu or L-pyro. One of the

421 major structural changes that occurs upon excitation is an increase in the C=O bond length

422 similar to observations in previous studies (*38–40*). Fig. 4c shows the oscillator strengths as

423 a function of the C=O bond, that increases in length by about 0.1 Angstroms.

424

425 Although all three glutamine-related structures display similar trends on the excited state,

426 what makes L-pyro-amm unique is the presence of the SHB. Fig. 4b and c show that L-pyro-

427 amm displays the largest oscillator strength peaking at approximately 3.5eV consistent with

428 our experimental findings. Although L-glu also has a peak at around 3.5 eV it is much weaker

16

429   than the one of L-pyro-amm. We thus decided to focus on a series of excited state

430   optimisations for various clusters of L-pyro-amm. In particular, we focused on the proton

431   transfer in the ground state as seen in the double-well potential and on the proximity of the

432   ammonium ion to the short hydrogen bond region, all shown to play an important role in

433   the optical properties of L-pyro-amm so far. We thus constructed three clusters with

434   different initial conditions, which are shown in the top panels of Fig. 4d-f. The clusters

435   shown in Fig. 4d and 4e differ in the initial positions of the protons along the SHB. As seen in

436   Fig. 4a, the ground-state simulations of L-pyro-amm present a double-well potential in the

437   finite temperature simulations. We thus moved the proton along one of the SHBs,

438   constrained the geometry in the ground-state which yielded the cluster shown in Fig. 4e. In

439   Fig. 4f, the ammonium ion is placed closer to the SHB region.

440

441   The circled regions in Fig. 4d-f highlight the main regions, where the nuclear degrees of

442   freedom respond in the excited state. The bottom panels show a zoomed in image of the

443   changes that occur upon relaxation, for which the solid and transparent structures

444   correspond to geometries obtained before and after the relaxation on the excited state,

445   respectively. The bottom panel of Fig. 4d illustrates that the change involves the C=O stretch

446   and deplanarisation of the peptide dihedral angle of the ring. The corresponding evolution

447   of the first excited state and ground state energies as a function of optimisation is shown in

448   Fig. 4g. The relaxation on the excited state narrows the energy difference between the

449   ground and excited state to approximately 3.5eV which is consistent with the experiments.

450

451   The top panels of Fig. 4e and f involve two other initial conditions for which the proton

452   vibrations and the proximity of the ammonium ion to the SHB are altered. We see in Fig. 4h

453   and i that the magnitude of the oscillator strength of L-pyro-amm in the excited state is

454   sensitive to these new initial conditions. Transferring the protons on the ground-state (see

455   dotted black rectangles in Fig. 4d-f), significantly changes the oscillator strengths as seen in

456   the comparison between Fig. 4g-i, across the entire relaxation process in the first excited

457   state while still maintaining the C=O stretch and deplanarisation as seen in the bottom

458   panel of Fig. 3e. In the case of Fig. 4f, besides the reorganisation involving the C=O stretch,

459   we also observe a proton transfer along the SHB. This is seen in Fig. 4i, which shows the O-H

460   stretch (dashed-blue curve) along the SHB during the optimisation which increases from

461 1.26 to 1.32 Angstroms. The zoomed in plot in the bottom panel of Fig. 4f shows this subtle

462 change in the proton transfer coordinate. Thus, the evolution of the excited state in L-pyro-

463 amm into the region displaying visible fluorescence appears to involve a collective

464 reorganisation of various vibrational modes forming the hydrogen bond network with the

465 SHB playing a particular role, as it leads to the brightest structure, also confirmed

466 experimentally. These findings are also consistent with some recent theoretical work

467 showing the importance of proton transfer in self-assembled peptides made of aromatic

468 phenyl-alanine amino acids (41). However, the latter structure features an aromatic amino

469 acid, whereas we observe similar optical properties in non-aromatic structures.

470

471 **Conclusions**

472

473 The experimental and theoretical findings presented here, elucidate a rather complex

474 molecular mechanism associated with the non-aromatic intrinsic fluorescence in protein-

475 like structures. In the case of L-glutamine, a chemical reaction creates a newly formed

476 structure involving a cyclised pyroglutamic acid ring. This new structure features absorption

477 in the UV and emission in the visible range very similar to the chemically distinct amyloid

478 fibrils (4, 5, 11, 12, 41–43).

479

480 The structural chromophore responsible for the optical properties in this new protein-

481 related structure arises from a hydrogen bond network characterised by specific vibrational

482 fluctuations on the excited state. The presence of strong hydrogen bonds along which

483 proton transfer occurs and secondly, specific ionic interactions in close proximity, such as

484 involving the ammonium ion, affect the optical properties. Although the fluorescence

485 observed in these systems is much weaker than those compared to conventional

486 fluorophores, the physical and chemical properties of the hydrogen bond network reported

487 here maybe a generic feature across many other peptide structures.

488

489 In summary, we show here that there are several vibrational modes in biological structures

490 that contribute to fluorescence properties as shown by excited state simulations and

491 confirmed experimentally. We further show that the protein environment strongly

492 contributes to the optical activity of the protein like structure and that the SHB significantly

18

493 enhances the fluorescence signal detected, potentially by inhibiting a conical intersection in
494 the excited state as discussed previously (5). Interestingly, SHBs have recently been
495 observed in different biological systems which have long been associated with either
496 intrinsic fluorescence, such as NADP/NAD (44), FAD/FMN (45), the light-sensing
497 chromophore in photoactive yellow protein (46), or in the active site of many enzymes, such
498 as hydrolases and oxidoreductases (47, 48), many of which consist of a highly complex H-
499 bond structure similar to amyloid proteins. Our findings may thus further the design of
500 novel optically active biomaterial for applications in optical sensing or the design of novel
501 biocompatible catalysts.
502

503 **Author Information**
504 **Corresponding Authors**
505 Ali A. Hassanali, ahassana@ictp.it
506 Gabriele S. Kaminski Schierle, gsk20@cam.ac.uk
507

508 **Author Contributions**
509 *A.D.S and M.N.Q contributed equally. A.D.S, prepared samples for all experimental data.
510 P.J.W. performed SEM experiments. A.D.B and M.T.R performed XRD measurements and
511 analysed data. M.T.R. performed THz experiments and DFT-THz calculations and analysed
512 data. A.D.S. performed excitation and emission measurements and analysed data. A.D.S and
513 S.T.J. performed absorption measurements and analysed data. M.T.R and E.M.K performed
514 TD-DFT cluster calculations. M.N.Q, E.P, L.G, R.G and A.H performed AIMD, Periodic TD-DFT
515 Excited State Calculations and Periodic Structure Geometry Optimisation calculations. A.D.S,
516 M.N.Q, M.T.R, S.T.J, L.G, J.A.Z, D.C, A.H and G.S.K.S contributed to manuscript writing. All
517 authors have given approval to the final version of the manuscript.
518

519 **Notes**
520 The authors declare no competing financial interest.
521

19

527

528

529

530

531

532

533

534

535 **Supplementary data**
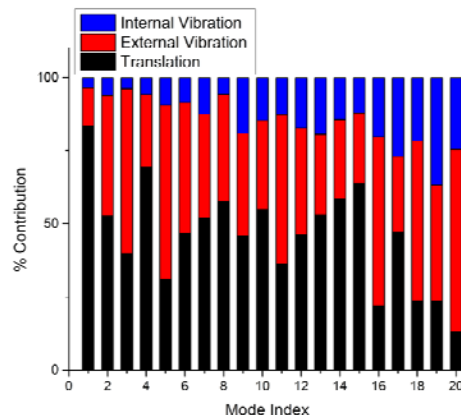
| Mode Number	Frequency (THz)	Intensity (km mol⁻¹)	Assignment
1	0.955	0.22	Antisymmetric translation in b
2	1.215	0.71	Coupled translation in a and rotation about bc
3	1.325	1.52	external rotation about b
4	1.450	0.36	Asymmetric translation in c
5	1.554	4.37	External rotation about a
6	1.676	1.76	Translation in a and external asymmetric rotation about H-bond coordinate
7	1.805	2.28	External asymmetric rotation of dimer pairs
8	1.929	2.11	External symmetric rotation of dimer pairs
9	1.950	1.28	Asymmetric rotation about h-bond coordinate, ammonium translational motion
10	2.113	3.53	Translation and rotation (breathing) around ammonium cation
11	2.208	2.5	Symmetric external rotation of entire formula units
12	2.404	2.37	In phase external rotation perpendicular to h-bond coordinate
13	2.502	0.45	Out of phase external rotataion perpendicular to h-bond coordinate
14	2.564	0.73	External out of phase rotation of h-bonded chains about b
15	2.565	8.91	Out of phase external rotation of individual pyroglutamic molecules with translation of ammonium cation
16	2.654	18.09	External vibration coupled with torsion of the COOH group
17	2.679	0.29	External rotation and torsion of pyroglutamic ring
18	2.776	4.94	External rotation and torsion of ring and carboxyl group
19	2.988	2.68	External rotataion and translation of ammonium

536

537 **Supplementary Figure 1. Full spectral assignment of THz data.**

538 The top chart shows the contribution to each IR-active mode including external translations

539 and hindered rotations, and internal vibrational motions (i.e. torsions), while the bottom

540 table lists the detailed assignment for each mode.

541

542

543
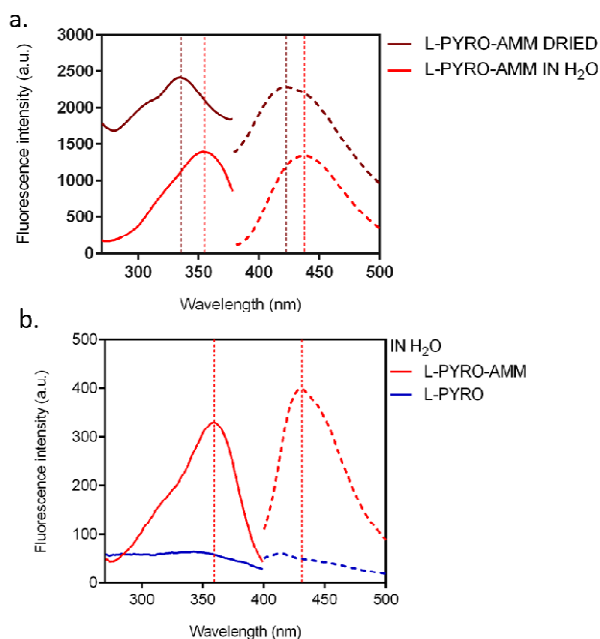
Supplementary Figure 2. L-pyro-amm has blue shifted fluorescence when dried and displays higher fluorescence intensity than L-pyro.

(a)The excitation peak of L-pyro-amm when dried (solid dark red line) is blue shifted with a peak maximum ~ 340 nm compared to L-pyro-amm in H_2O (solid red line) which has a peak maximum ~ 360 nm. The emission peak of L-pyro-amm when dried (dashed dark red line) is also blue shifted, with a peak maximum ~ 420 nm, compared to L-pyro-amm in H_2O (dashed red line) with a peak maximum ~ 430 nm. (b) 1 M L-glu and 1 M L-pyro (blue) were incubated in H_2O for 8 days at 65°C. After 9 days, the L-glu had converted into the L-pyro-amm structure (red). L-pyro-amm has a clear excitation peak maximum at ~360 nm and emission peak maximum at ~ 430 nm, while L-pyro (blue), although not completely dark, has no clear excitation or emission peak.
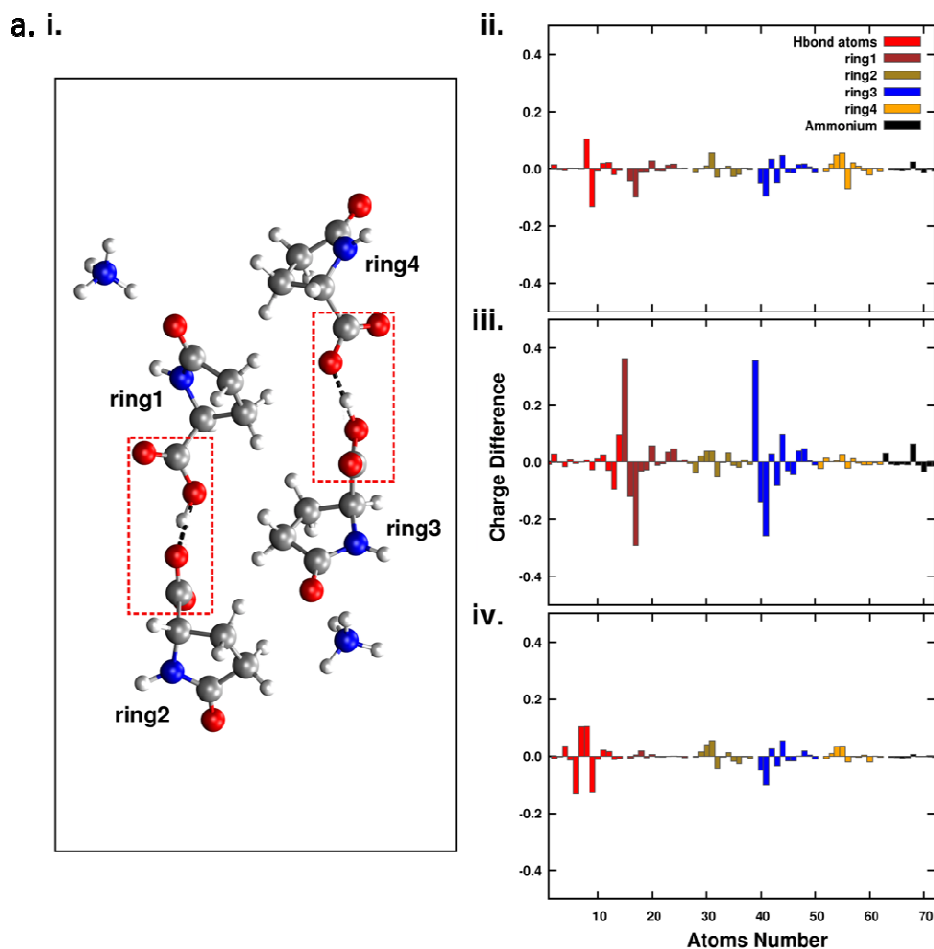
Supplementary Figure 3. The optical properties of L-pyro-amm are sensitive to the environment and involves the electronic response of the entire structure.

(a)(i) L-pyro-amm cluster used to examine the sensitivity of the optical response on different parts of the cluster upon moving different protons. (ii) Charge differences between the ground and excited state are computed using restrained electrostatic potential atomic partial charges (RESP) for the cluster shown in i). Note, the electronic response involves all the atoms of the cluster. (iii) The two protons in the rectangle regions are displaced to be in the centre of the hydrogen bond and the charge differences are then computed. As illustrated, the proton displacement leads to a larger change in magnitude of the charges. (iv) The charge differences are computed for another nuclear configuration for which the protons are kept fixed but the $O—O$ distance is increased from 2.45 to 3.2 Angstroms. The charge differences obtained here are quite similar to the original condition shown in (ii).

570   **References:**

571   1.   A. Shukla, S. Mukherjee, S. Sharma, V. Agrawal, K. V. R. Kishan, P. Guptasarma, A

572   novel UV laser-induced visible blue radiation from protein crystals and aggregates:

573   Scattering artifacts or fluorescence transitions of peptide electrons delocalized

574   through hydrogen bonding? *Arch. Biochem. Biophys.* **428**, 144–153 (2004).

575   2.   G. Rosenman, N. Amdursky, M. Molotskii, D. Aronov, L. Adler-Abramovich, E. Gazit,

576   Blue luminescence based on quantum confinement at peptide nanotubes. *Nano Lett.*

577   **9**, 3111–3115 (2009).

578   3.   F. T. Chan, D. Pinotsi, G. S. K. Schierle, C. F. Kaminski, in *Bio-nanoimaging: Protein*

579   *Misfolding and Aggregation* (Elsevier, 2013;

580   http://linkinghub.elsevier.com/retrieve/pii/B9780123944313000134), pp. 147–155.

581   4.   F. T. S. Chan, G. S. Kaminski Schierle, J. R. Kumita, C. W. Bertoncini, C. M. Dobson, C. F.

582   Kaminski, C. V Robinson, C. M. Dobson, J. Beard, P. Das, K. Jansen, M. DeLucia, W.-L.

583   Lin, G. Dolios, R. Wang, C. B. Eckman, D. W. Dickson, M. Hutton, J. Hardy, T. Golde,

584   Protein amyloids develop an intrinsic fluorescence signature during aggregation.

585   *Analyst.* **138**, 2156 (2013).

586   5.   D. Pinotsi, L. Grisanti, P. Mahou, R. Gebauer, C. F. Kaminski, A. Hassanali, G. S.

587   Kaminski Schierle, Proton Transfer and Structure-Specific Fluorescence in Hydrogen

588   Bond-Rich Protein Structures. *J. Am. Chem. Soc.* **138**, 3046–3057 (2016).

589   6.   J. Pansieri, V. Josserand, S. J. Lee, A. Rongier, D. Imbert, M. M. Sallanon, E. Kövari, T.

590   G. Dane, C. Vendrely, O. Chaix-Pluchery, M. Guidetti, J. Vollaire, A. Fertin, Y. Usson, P.

591   Rannou, J. L. Coll, C. Marquette, V. Forge, Ultraviolet–visible–near-infrared optical

592   properties of amyloid fibrils shed light on amyloidogenesis. *Nat. Photonics.* **13**, 473–

593   479 (2019).

594   7.   L. Adler-Abramovich, E. Gazit, Correction: The physical properties of supramolecular

595   peptide assemblies: From building block association to technological applications.

596   *Chem. Soc. Rev.* **43**, 7236–7236 (2014).

597   8.   L. Adler-Abramovich, M. Reches, V. L. Sedman, S. Allen, S. J. B. Tendler, E. Gazit,

598   Thermal and chemical stability of diphenylalanine peptide nanotubes: Implications for

599   nanotechnological applications. *Langmuir.* **22**, 1313–1320 (2006).

600   9.   K. Tao, P. Makam, R. Aizen, E. Gazit, Self-assembling peptide semiconductors. *Science*

601   *(80-.).* **358** (2017), p. eaam9756.

602 10. J. M. Andresen, J. Gayán, L. Djoussé, S. Roberts, D. Brocklebank, S. S. Cherny, L. R.

603   Cardon, J. F. Gusella, M. E. Macdonald, R. H. Myers, D. E. Housman, N. S. Wexler, J.

604   Lorimer, J. Porter, F. Gomez, C. Moskowitz, K. P. Gerstenhaber, E. Shackell, K. Marder,

605   G. Penchaszadeh, S. A. Roberts, A. Brickman, D. Brocklebank, J. Gray, S. R. Dlouhy, S.

606   Wiktorski, M. E. Hodes, P. M. Conneally, J. B. Penney, J. F. Gusella, J. H. Cha, M.

607   Irizarry, D. Rosas, S. Hersch, Z. Hollingsworth, A. B. Young, D. E. Housman, M. M. de

608   Young, E. Bonilla, T. Stillings, A. Negrette, S. R. Snodgrass, M. D. Martinez-Jaurrieta,

609   M. A. Ramos-Arroyoh, J. Bickham, J. S. Ramos, F. Marshall, I. Shoulson, G. J. Rey, A.

610   Feigin, N. Arnheim, A. Acevedo-Cruz, L. Acosta, J. Alvir, K. Fischbeck, L. M. Thompson,

611   A. Young, L. Dure, C. J. O'Brien, J. Paulsen, S. P. Moran, D. Krch, P. Hogarth, D. S.

612   Higgins, B. Landwehrmeyer, M. R. Hayden, E. W. Almqvist, R. R. Brinkman, O.

613   Suchowersky, A. Durr, C. C. Dodé, F. Squitieri, P. J. Morrison, M. Nance, C. A. Ross, R.

614   L. Margolis, A. Rosenblatt, G. T. Estrella, D. M. Cabrero, R. J. A. Trent, E. McCusker, A.

615   Novelletto, M. Frontali, J. S. Paulsen, R. Jones, A. Zanko, T. Ashizawa, A. Lazzarini, J. L.

616   Li, V. C. Wheeler, A. L. Russ, G. Xu, J. S. Mysore, T. Gillis, M. Hakky, L. A. Cupples, M.

617   Saint-Hilaire, S. M. Hersch, The relationship between CAG repeat length and age of

618   onset differs for Huntington's disease patients with juvenile onset or adult onset.

619   *Ann. Hum. Genet.* **71**, 295–301 (2007).

620 11. D. Pinotsi, A. K. Buell, C. M. Dobson, G. S. Kaminski Schierle, C. F. Kaminski, A Label-

621   Free, Quantitative Assay of Amyloid Fibril Growth Based on Intrinsic Fluorescence.

622   *ChemBioChem.* **14**, 846–850 (2013).

623 12. T. N. Tikhonova, N. R. Rovnyagina, A. Y. Zherebker, N. N. Sluchanko, A. A. Rubekina, A.

624   S. Orekhov, E. N. Nikolaev, V. V. Fadeev, V. N. Uversky, E. A. Shirshin, Dissection of the

625   deep-blue autofluorescence changes accompanying amyloid fibrillation. *Arch.*

626   *Biochem. Biophys.* **651**, 13–20 (2018).

627 13. H. Mori, K. Takio, M. Ogawara, D. J. Selkoe, Mass spectrometry of purified amyloid β

628   protein in Alzheimer's disease. *J. Biol. Chem.* **267**, 17082–17086 (1992).

629 14. M. Fändrich, C. M. Dobson, The behaviour of polyamino acids reveals an inverse side

630   chain effect in amyloid structure formation. *EMBO J.* **21**, 5682–90 (2002).

631 15. R. Dovesi, A. Erba, R. Orlando, C. M. Zicovich-Wilson, B. Civalleri, L. Maschio, M. Rérat,

632   S. Casassa, J. Baima, S. Salustro, B. Kirtman, Quantum-mechanical condensed matter

633   simulations with CRYSTAL. *Wiley Interdiscip. Rev. Comput. Mol. Sci.* **8**, e1360 (2018).

634   16.   P. Giannozzi, O. Andreussi, T. Brumme, O. Bunau, M. Buongiorno Nardelli, M.

635   Calandra, R. Car, C. Cavazzoni, D. Ceresoli, M. Cococcioni, N. Colonna, I. Carnimeo, A.

636   Dal Corso, S. De Gironcoli, P. Delugas, R. A. Distasio, A. Ferretti, A. Floris, G. Fratesi, G.

637   Fugallo, R. Gebauer, U. Gerstmann, F. Giustino, T. Gorni, J. Jia, M. Kawamura, H. Y. Ko,

638   A. Kokalj, E. Kücükbenli, M. Lazzeri, M. Marsili, N. Marzari, F. Mauri, N. L. Nguyen, H.

639   V. Nguyen, A. Otero-De-La-Roza, L. Paulatto, S. Poncé, D. Rocca, R. Sabatini, B. Santra,

640   M. Schlipf, A. P. Seitsonen, A. Smogunov, I. Timrov, T. Thonhauser, P. Umari, N. Vast,

641   X. Wu, S. Baroni, Advanced capabilities for materials modelling with Quantum

642   ESPRESSO. *J. Phys. Condens. Matter*. **29** (2017), doi:10.1088/1361-648X/aa8f79.

643   17.   M. T. Ruggiero, J. Gooch, J. Zubieta, T. M. Korter, Evaluation of Range-Corrected

644   Density Functionals for the Simulation of Pyridinium-Containing Molecular Crystals. *J.*

645   *Phys. Chem. A*. **120**, 939–947 (2016).

646   18.   J. Da Chai, M. Head-Gordon, Long-range corrected hybrid density functionals with

647   damped atom-atom dispersion corrections. *Phys. Chem. Chem. Phys.* **10**, 6615–6620

648   (2008).

649   19.   D. Rocca, R. Gebauer, Y. Saad, S. Baroni, Turbo charging time-dependent density-

650   functional theory with Lanczos chains. *J. Chem. Phys.* **128** (2008),

651   doi:10.1063/1.2899649.

652   20.   N. Troullier, J. L. Martins, Efficient pseudopotentials for plane-wave calculations.

653   *Phys. Rev. B*. **43**, 1993–2006 (1991).

654   21.   A. D. Becke, Density-functional thermochemistry. III. The role of exact exchange. *J.*

655   *Chem. Phys.* **98**, 5648–5652 (1993).

656   22.   J. D. Head, M. C. Zerner, A Broyden-Fletcher-Goldfarb-Shanno optimization procedure

657   for molecular geometries. *Chem. Phys. Lett.* **122**, 264–270 (1985).

658   23.   J. VandeVondele, M. Krack, F. Mohamed, M. Parrinello, T. Chassaing, J. Hutter,

659   Quickstep: Fast and accurate density functional calculations using a mixed Gaussian

660   and plane waves approach. *Comput. Phys. Commun.* **167**, 103–128 (2005).

661   24.   S. Goedecker, M. Teter, Separable dual-space Gaussian pseudopotentials. *Phys. Rev.*

662   *B - Condens. Matter Mater. Phys.* **54**, 1703–1710 (1996).

663   25.   A. D. Becke, Density-functional exchange-energy approximation with correct

664   asymptotic behavior. *Phys. Rev. A*. **38**, 3098–3100 (1988).

665   26.   S. Grimme, J. Antony, S. Ehrlich, H. Krieg, A consistent and accurate *ab initio*

666   parametrization of density functional dispersion correction (DFT-D) for the 94

667   elements H-Pu. *J. Chem. Phys.* **132**, 154104 (2010).

668   27.   G. Bussi, D. Donadio, M. Parrinello, Canonical sampling through velocity rescaling. *J.*

669   *Chem. Phys.* **126** (2007), doi:10.1063/1.2408420.

670   28.   T. Yanai, D. P. Tew, N. C. Handy, A new hybrid exchange-correlation functional using

671   the Coulomb-attenuating method (CAM-B3LYP). *Chem. Phys. Lett.* **393**, 51–57 (2004).

672   29.   K. Jong, Y. Taghipour Azar, L. Grisanti, A. D. Stephens, S. T. E. Jones, D. Credgington, G.

673   S. Kaminski Schierle, A. A. Hassanali, Low Energy Optical Excitations as an Indicator of

674   Structural Changes Initiated at the Termini of Amyloid Protein. *Phys. Chem. Chem.*

675   *Phys.* (2019), doi:10.1039/c9cp04648h.

676   30.   L. Grisanti, D. Pinotsi, R. Gebauer, G. S. Kaminski Schierle, A. A. Hassanali, A

677   computational study on how structure influences the optical properties in model

678   crystal structures of amyloid fibrils. *Phys. Chem. Chem. Phys.* **19**, 4030–4040 (2017).

679   31.   E. P. J. Parrott, J. A. Zeitler, Terahertz time-domain and low-frequency Raman

680   spectroscopy of organic materials. *Appl. Spectrosc.* **69**, 1–25 (2015).

681   32.   Y. K. Law, A. A. Hassanali, Role of Quantum Vibrations on the Structural, Electronic,

682   and Optical Properties of 9-Methylguanine. *J. Phys. Chem. A.* **119**, 10816–10827

683   (2015).

684   33.   S. Sappati, A. Hassanali, R. Gebauer, P. Ghosh, Nuclear quantum effects in a

685   HIV/cancer inhibitor: The case of ellipticine. *J. Chem. Phys.* **145** (2016),

686   doi:10.1063/1.4968046.

687   34.   Y. K. Law, A. A. Hassanali, The importance of nuclear quantum effects in spectral line

688   broadening of optical spectra and electrostatic properties in aromatic chromophores.

689   *J. Chem. Phys.* **148** (2018), doi:10.1063/1.5005056.

690   35.   D. Marx, Erratum: Proton transfer 200 years after von grotthuss: Insights from Ab

691   initio simulations (ChemPhysChem (2006) 7 (1848-1810)). *ChemPhysChem.* **8**, 209–

692   210 (2007).

693   36.   S. Prasad, I. Mandal, S. Singh, A. Paul, B. Mandal, R. Venkatramani, R. Swaminathan,

694   Near UV-Visible electronic absorption originating from charged amino acids in a

695   monomeric protein. *Chem. Sci.* **8**, 5416–5433 (2017).

696   37.   I. Mandal, S. Paul, R. Venkatramani, Optical backbone-sidechain charge transfer

697   transitions in proteins sensitive to secondary structure and modifications. *Faraday*

698 *Discuss.* **207**, 115–135 (2018).

699 38. M. Mališ, Y. Loquais, E. Gloaguen, H. S. Biswal, F. Piuzzi, B. Tardivel, V. Brenner, M.

700 Broquier, C. Jouvet, M. Mons, N. D. S. Došlić, I. Ljubić, Unraveling the mechanisms of

701 nonradiative deactivation in model peptides following photoexcitation of a

702 phenylalanine residue. *J. Am. Chem. Soc.* **134**, 20340–20351 (2012).

703 39. B. P. Fingerhut, K. E. Dorfman, S. Mukamel, Monitoring nonadiabatic dynamics of the

704 RNA base uracil by UV pump-IR probe spectroscopy. *J. Phys. Chem. Lett.* **4**, 1933–

705 1942 (2013).

706 40. M. Sapunar, T. Ayari, N. Došlić, Comparative study of the photodynamics of

707 malonaldehyde and acetylacetone. *Chem. Phys.* **515**, 622–627 (2018).

708 41. S. K. Joseph, N. Kuritz, E. Yahel, N. Lapshina, G. Rosenman, A. Natan, Proton-Transfer-

709 Induced Fluorescence in Self-Assembled Short Peptides. *J. Phys. Chem. A.* **123**, 1758–

710 1765 (2019).

711 42. A. Handelman, N. Kuritz, A. Natan, G. Rosenman, Reconstructive Phase Transition in

712 Ultrashort Peptide Nanostructures and Induced Visible Photoluminescence.

713 *Langmuir*. **32** (2016), pp. 2847–2862.

714 43. L. L. Del Mercato, P. P. Pompa, G. Maruccio, A. Della Torre, S. Sabella, A. M.

715 Tamburro, R. Cingolani, R. Rinaldi, Charge transport and intrinsic fluorescence in

716 amyloid-like fibrils. *Proc Natl Acad Sci U S A.* **104**, 18019–18024 (2007).

717 44. A. Stavrinides, E. C. Tatsis, L. Caputi, E. Foureau, C. E. M. Stevenson, D. M. Lawson, V.

718 Courdavault, S. E. O'Connor, Structural investigation of heteroyohimbine alkaloid

719 synthesis reveals active site elements that control stereoselectivity. *Nat. Commun.* **7**

720 (2016), doi:10.1038/ncomms12116.

721 45. F. Forneris, D. P. H. M. Heuts, M. Delvecchio, S. Rovida, M. W. Fraaije, A. Mattevi,

722 Structural analysis of the catalytic mechanism and stereoselectivity in Streptomyces

723 coelicolor alditol oxidase. *Biochemistry*. **47**, 978–985 (2008).

724 46. S. Yamaguchi, H. Kamikubo, K. Kurihara, R. Kuroki, N. Niimura, N. Shimizu, Y.

725 Yamazaki, M. Kataoka, Low-barrier hydrogen bond in photoactive yellow protein.

726 *Proc. Natl. Acad. Sci. U. S. A.* **106**, 440–444 (2009).

727 47. W. W. Cleland, P. A. Frey, J. A. Gerlt, The low barrier hydrogen bond in enzymatic

728 catalysis. *J. Biol. Chem.* **273** (1998), pp. 25529–25532.

729 48. S. Zhou, L. Wang, Unraveling the structural and chemical features of biological short

730   hydrogen bonds. *Chem. Sci.* **10**, 7734–7745 (2019).

731